NUMERICAL SIMULATION STUDY OF GAS-SOLID TWO-PHASE FLOW IN BEARING DUST COVER

Xiaochen WU[2], Guangbin DUAN*[2], Qingxin ZHAO[1], Dongmei CAI[1], Bing LV[1], Wenzhen ZHONG[1, *]

This study proposed a novel bearing dust cover to address the limited dustproof performance of current designs. CFD-DEM simulations of gas-solid flow in the standard bearing cover revealed axial airflow velocity as the primary dustproof failure cause, prompting the development of a fan-shaped dust cover. Numerical simulations and material experiments were performed on the novel bearing cover. The simulation demonstrated that the optimized cover achieves internal airflow recirculation, effectively preventing external particles entering the bearing cavity under the effect of filter mesh. The experiment results showed good agreement with numerical simulations. Under identical operating conditions, bearing with the standard cover exhibited 20,120 particles/cm³ contamination density, whereas fan-shaped covers reduced contamination by 93%. Development of the novel dust cover significantly improves dustproof performance, thereby extending the bearing's service life.

Keywords: Bearing dust cover; CFD-DEM coupling; Dustproof performance simulation; Gas-solid two-phase flow

1. Introduction

Dustproof performance of bearings has always been a technical challenge in design and production [1]. The bearing dust cover, crucial for preventing external particulate ingress into the bearing cavity under various conditions to ensure smooth bearing operation [2]. Currently, the most widely used rolled-edge dust covers are extensively applied in industrial fields such as mining, building materials, and chemical industries [3]. However, standard dust covers exhibit poor environmental adaptability, and bearings operating in dust-laden environments still experience abrasive wear due to the ingress of substantial amounts of dust particles into the bearing cavity [4-5]. Numerous researchers have used computational fluid dynamics (CFD) to analyze the internal flow and particle fields of bearings. Feng [6] et al. investigated the motion and deposition patterns of submicron particles in gyro motor bearings. Wang [7] et al. used volume of

[1]School of Mechanical Engineering, University of Jinan, China
[2]School of Materials Science and Engineering, University of Jinan, China
*Corresponding authors email: me_zhongwz@ujn.edu.cn and mse_duangb@ujn.edu.cn

(VOF) model to analyze the effects of bearing speed and lubricant supply rate on internal fluid motion. Chen [8] et al. conducted a dispersed phase model (DPM) analysis on liquid hybrid bearings under constant operating conditions, investigating the effects of impurity particle mass fraction and particle diameter on the load-carrying capacity of the water film. When the particle size approached the minimum film thickness, the maximum water film pressure and load-carrying capacity exhibited significant increases, while simultaneously intensifying frictional wear in the bearings. However, employing CFD alone can only investigate the one-way coupling effects of the flow field on particles, and is incapable of enabling two-way coupling analysis between the flow field and particle field, thereby resulting in significant deviations of simulation results from actual observations [9]. In recent years, the development of the computational fluid dynamics-discrete element method (CFD-DEM) has effectively solved this problem [10]. The CFD-DEM method comprehensively accounts for fluid-particle interactions and particle-particle interactions, which has been widely applied to dust-related fields. Wang [11] et al. employed the CFD-DEM method to investigate the spatial distribution patterns of dust movement during seeder operation. Their results demonstrated that airflow velocity exerted the most significant influence on dust concentration ($P<0.01$), followed by operational speed ($P<0.05$). By strategically relocating the air intake of the air-suction seed-metering device to low dust concentration zones, they effectively reduced inhalation risks. Zhang [12] et al. systematically analyzed the dynamic characteristics of gas-solid two-phase flow fields during grab bucket discharge using CFD-DEM coupled simulations. They proposed a novel dust suppression design methodology based on particle suspension velocity, providing critical insights for industrial dust control strategies. Feng [13] et al. conducted CFD-DEM simulations to examine coal particle motion in mining environments, revealing key distribution mechanisms. Their findings indicated an inverse correlation between particle velocity and diameter, with an observed accumulation angle of approximately 21° in cavity structures. These results further elucidate the transient destructive effects associated with dynamic outburst phenomena in coal seams.

Current research using CFD-DEM method has matured in studying dust diffusion mechanisms in open spaces, while investigations into bearing dustproof mechanisms in confined spaces have not yet been explored. This study establishes precise division of fluid domain and rotating domain based on actual operating conditions of bearing dust covers. The CFD-DEM numerical simulation of flow-particle interaction fields of standard dust covers was conducted, with investigative parameters focusing on the effects of bearing rotational speed and air inlet velocity on dustproof performance. And a rigorous analysis of internal gas-solid interaction mechanisms was conducted, elucidating the primary dustproof

failure cause in the standard bearing dust cover. The standard bearing dust cover structure was optimized by developing a new fan-shaped design. Numerical simulations and material experiments comparing dustproof performance between the standard cover and the fan-shaped cover provided theoretical guidance for further improvements. While CFD-DEM enables detailed analysis of dust ingress mechanisms in bearing seals, its excessive computational costs limit simulations to simplified particle distributions. Moreover, the absence of universally applicable drag models for confined rotating geometries contributes to inaccuracies in predicting particle deposition patterns. Future work will focus on enhancing computational efficiency and refining the gas-solid interaction model.

2. Numerical simulation of standard bearing dust cover

2.1 Mathematical model

In dust-proof processes, the flow field comprises a gas-solid multiphase system dominated by air (continuous phase) and dust particles (dispersed phase). Within the Eulerian-Lagrangian framework, the continuous-phase air is governed by the incompressible Navier-Stokes equations for Newtonian fluids, while discrete particles are tracked via Lagrangian mechanics. The conservation of mass and momentum for the continuous phase is rigorously expressed by eqs (1) and (2).

$$\frac{\partial}{\partial t}(\varepsilon_g \rho_g) + \nabla \cdot (\varepsilon_g \rho_g u_g) \& = 0 \tag{1}$$

$$\frac{\partial}{\partial t}(\varepsilon_g \rho_g u_g) + \nabla \cdot (\varepsilon_g \rho_g u_g) \& = -\varepsilon_g \nabla p + \nabla \cdot (\varepsilon_g \tau_g) + \varepsilon_g \rho_g g - F_{g-p} \tag{2}$$

In the equations, ε_g is the volume fraction of the air; ρ_g is the density of the air, kg/m³; u_g is the air velocity, m/s; τ_g is the viscous stress tensor of the air; g is the gravitational acceleration, 9.8 m/s^2; p is the pressure of the air, Pa; $F_{g\text{-}p}$ is the interphase interaction force between the particle and the air, N.

To more accurately predict turbulent flow and enhance numerical simulation precision, this study adopts the *RNG k-ε* model due to the presence of a significant amount of curved-wall separated flow and porous media flow inside the bearing dust cover. The transport equations governing the turbulent kinetic energy (k) and its dissipation rate (ε) are expressed by the semi-empirical conservation eqs (3) and (4).

$$\frac{\partial(\rho k)}{\partial t} + \frac{\partial(\rho k u_i)}{\partial x_i} = \frac{\partial}{\partial x_i}\left(\alpha_k \mu_{eff} \frac{\partial k}{\partial x_j}\right) + G_k + G_b - \rho\varepsilon - Y_M + S_k \tag{3}$$

$$\frac{\partial(\rho\varepsilon)}{\partial t}+\frac{\partial(\rho\varepsilon u_i)}{\partial x_i}=\frac{\partial}{\partial x_i}\left(\alpha_\varepsilon\mu_{eff}\frac{\partial\varepsilon}{\partial x_j}\right)+C_{1\varepsilon}\frac{\varepsilon}{k}(G_k+C_{3\varepsilon}G_b)-C_{2\varepsilon}\rho\frac{\varepsilon^2}{k}-R_\varepsilon+S_\varepsilon \quad (4)$$

In the equations, ρ is fluid density, kg/m³; k is turbulent kinetic energy, m²/s²; u_i is the fluid velocity, m/s; x_i , x_j are the distances in the i and j directions, m; α_k is the Prandtl number for turbulent kinetic energy; μ_{eff} is effective turbulent viscosity, Pa·s; G_k is turbulent kinetic energy generated by mean velocity gradients, m²/s²; G_b is turbulent kinetic energy generated by buoyancy, m²/s²; ε is turbulent energy dissipation rate, m²/s³; Y_M is the coefficient accounting for the effect of pulsation on total dissipation rate in compressible flows; S_k , S_ε are user-defined source terms; α_ε is the Prandtl number for turbulent dissipation rate; $C_{1\varepsilon}$, $C_{2\varepsilon}$, $C_{3\varepsilon}$ are empirical model coefficients; R_ε is the turbulent viscosity correction term for different Reynolds numbers.

In the bearing's rotating domain, dust particles are primarily subjected to gravity, drag, and buoyancy [14]. The dynamic behavior of the solid phase is governed by Newton's second law of motion. This formulation explicitly accounts for momentum transfer arising from inter-particle collisions and particle-boundary collisions. The translational motion of individual particles is described by eq. (5), while their rotational motion is governed by eq. (6).

$$m_p\frac{du_p}{dt}=m_pg+F_c+F_{p,g} \quad (5)$$

$$I_p\frac{d\omega_p}{dt}=\sum M_c \quad (6)$$

In the equations: u_p is the particle's linear velocity, m/s; m_p is the particle's mass, kg; F_c is the contact force during particle collisions, N; I_p is the particle's moment of inertia, kg·m^2; ω_p is the particle's angular velocity, rad/s; M_c is the contact torque, N·m; $F_{p,g}$ is the drag force between the particle and air, N.

2.2 Domain and mesh division of the standard bearing dust cover

The subject of this study is the SKF series standard bearing W6304-2Z. As shown in Fig. 1(a), its structure comprises an outer race, inner race, balls, cage and dust cover [15]. The flow field on one side of a standard bearing dust cover was selected as the simulation domain. As shown in Fig. 1(b), the dust cover structure is reasonably simplified to extract the fluid domain. The entire fluid domain consists of stationary domain and rotating domain with the brown wall being the interface. The sliding mesh method is employed to simulate the rotation of the inner race, with all other walls defined as stationary surfaces.

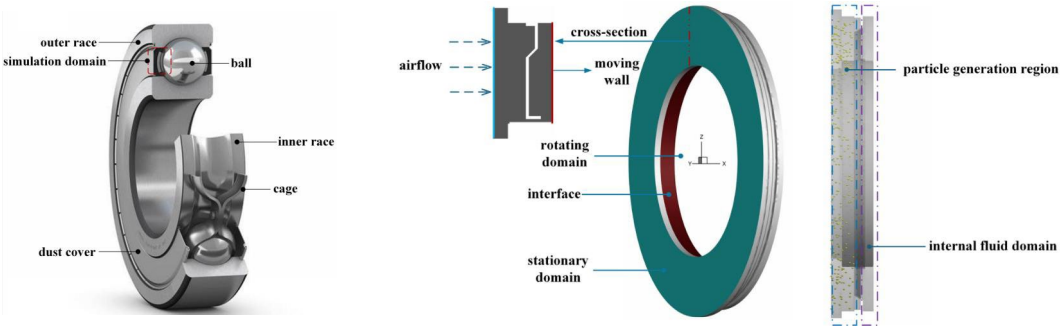

(a) Bearing structure (b) Dust Cover Fluid Domain division

Fig. 1 Geometric model of a standard bearing dust cover

After completing the solid modeling of the dust cover, Fluent Meshing was applied for mesh division. The mesh division is shown in Fig.2, with local refinement implemented along the inner wall surfaces of the rotating domain. The total number of mesh cells is 2,058,326, which ensures a stable distribution and meets the computational requirements.

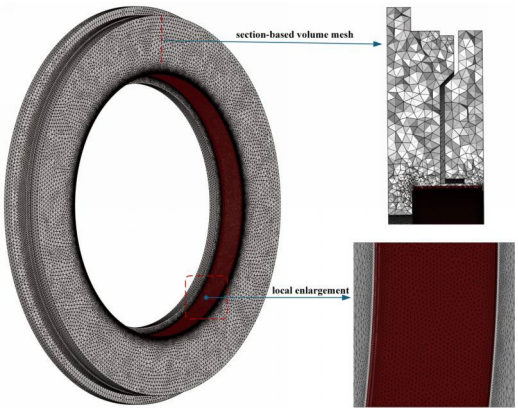

Fig. 2 Mesh division

2.3 Solution settings of the standard bearing dust cover

In Fluent, the geometric model and the numerical model maintain a closely interdependent relationship: The geometric model defines the spatial structure of the physical problem, while the numerical model mathematically solves the physical processes through discretization and algorithmic implementation. Particles are randomly generated in the external air domain shown in Fig.1(b). For other specific parameter settings, refer to Table. 1.

Table.1

Flow field and particle parameter settings of the standard bearing dust cover

Type	Item	Numerical value or Method
	Model	*RNG k-ε*
	Momentum	Second order upwind
	Wall	No slip
Flow field	Solver	Pressure-based
	Inlet	Velocity-inlet
	Outlet	Pressure-outlet
	Air inlet velocity (m/s)	0.001-0.01
	Rotational speed (rpm)	1000-2000
Particle	Size (m)	4.5×10^{-5}
	Density (kg/m^3)	3900
	Shear modulus (MPa)	1×10^4
	Poisson's ratio	0.25
Wall	Density (kg/m^3)	7850
	Shear modulus (MPa)	8×10^4
	Poisson's ratio	0.31
Particle-particle	Coefficient of restitution	0.5
	Coefficient of static firction	0.5
	Coefficient of rolling firction	0.01
Particle-wall	Coefficient of restitution	0.5
	Coefficient of static firction	0.6
	Coefficient of rolling firction	0.05

2.4 Influence of rotational speed and air inlet velocity on dustproof performance

Based on the constructed geometric and numerical models of the bearing dust cover, the analysis focuses on the most critical parameter: the number of particles entering the bearing cavity.

The particle concentration in the simulation environment was set to 2 g/m³ according to actual conditions [16]. To investigate the influence of rotational speed on dustproof performance of the standard bearing cover, this study conducted single-factor simulations with air inlet velocity maintained at 0.005 m/s while varying bearing speeds at 1000 rpm, 1500 rpm, and 2000 rpm.

As shown in Fig.3(a), with constant air inlet velocity and external dust concentration, the number of particles invading the bearing cavity decreases with increasing rotational speed. As the bearing rotational speed increases, the

intensified airflow induced by inner race rotation enhances centrifugal forces on airborne dust particles, accelerating their settling velocity. Consequently, more particles become deposited at the bearing bottom under combined centrifugal and gravitational effects. The entry of particles into the bearing cavity is predominantly concentrated within the first 0.25 s, the number of particles entering the chamber reaches a steady-state equilibrium thereafter. This stabilization arises because most particles have already settled to base of the bearing cavity under gravity within approximately 0.25 s, with only minimal particles subsequently entering the cavity through inner race-induced airflow.

To investigate the influence of air inlet velocity on dustproof performance of the standard bearing cover, this study established a bearing rotational speed of 1000 rpm and selected air inlet velocities of 0.001 m/s, 0.005 m/s, and 0.01 m/s.

As shown in Fig.3(b), with constant bearing rotational speed and external dust concentration, the number of particles invading the bearing cavity increases with increasing air inlet velocity. An increase in air inlet velocity induces turbulence in the internal flow field and enhances the drag force on dust particles. Dust particles exhibit increased horizontal displacement under identical settling durations. Particularly when air inlet velocity reaches 0.01m/s, dust particles can more easily penetrate the dust cover into the bearing cavity, with quantities approaching 100, which is 4 to 5 times higher than other conditions.

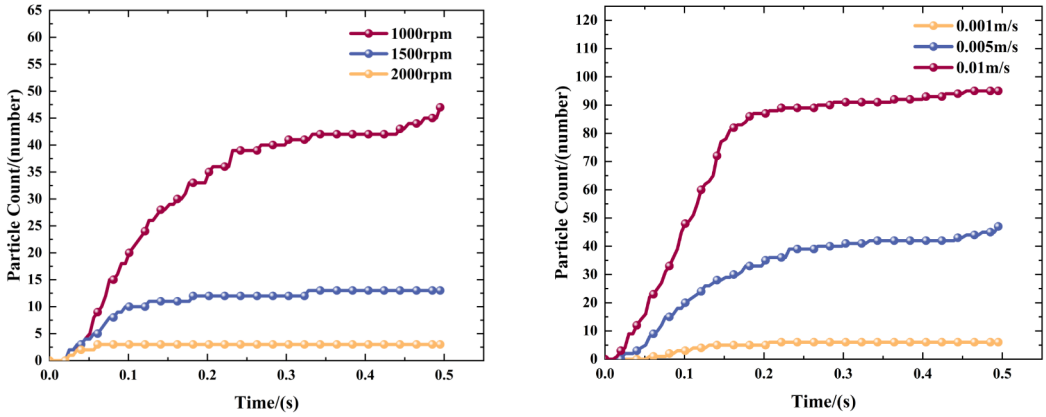

(a) Particle count in the bearing cavity under different rotational speeds

(b) Particle count in the bearing cavity under different air inlet velocities

Fig.3 Influence of rotational speed and air inlet velocity on dustproof performance

To validate the accuracy of the aforementioned conclusions, a sensitivity analysis was conducted in SPSSAU using bearing rotational speed and air inlet velocity as independent variables, with particle ingress count into bearings as the response target. The factor settings are detailed in Table 2, while the experimental design and corresponding results are presented in Table 3.

Table. 2

Levels of experimental factors

Bearing rotational speed A/(rpm)	Air inlet velocity B/(m/s)
1000	0.001
1500	0.005
2000	0.01

Table. 3

Experimental design and results

Number	A	B	Particle count in the bearing cavity
1	1000	0.001	15
2	1000	0.005	50
3	1000	0.01	322
4	1500	0.001	5
5	1500	0.005	12
6	1500	0.01	100
7	2000	0.001	3
8	2000	0.005	5
9	2000	0.01	59

Analysis of variance (ANOVA) of the regression model (Table 4) indicated that Factor B (air inflow velocity) exerted a significant effect ($p<0.05$) on particle ingress quantity into the bearing. Conversely, the effect of Factor A (bearing rotation speed) is not significant ($p>0.05$). These results confirm that both parameters influence dust cover failure mechanisms, with air inflow velocity exhibiting the dominant effect.

Table. 4

ANOVA for regression models

Sources of variation	*P*-value
A	0.113
B	0.034

2.5 Failure mechanism of standard bearing dust cover

The increasing air velocity results in more dust particles being entrained into the bearing cavity. To investigate the failure mechanisms of the standard dust cover, a detailed analysis of gas-solid interactions in the radial cross-section of the bearing was conducted. As shown in Fig.4, the black spheres represent dust particles, while the arrows indicate the air direction. At t=0 s, dust particles are generated in the external air domain of the dust cover, with no particles present in the bearing cavity. At t=0.2 s, most particles settle under gravitational force while approaching the bearing cavity under effects of airflow drag force. The complex flow field distribution surrounding the bearing prolongs particle residence time.

When the airflow demonstrates substantial axial velocity components, this induces significant horizontal displacement of dust particles, preventing timely sedimentation in external domain. The velocity near the clearance is significantly higher, and a small portion of the dust particles concentrated will gradually penetrate into the bearing cavity under the effect of the airflow, leading to the failure of dustproof.

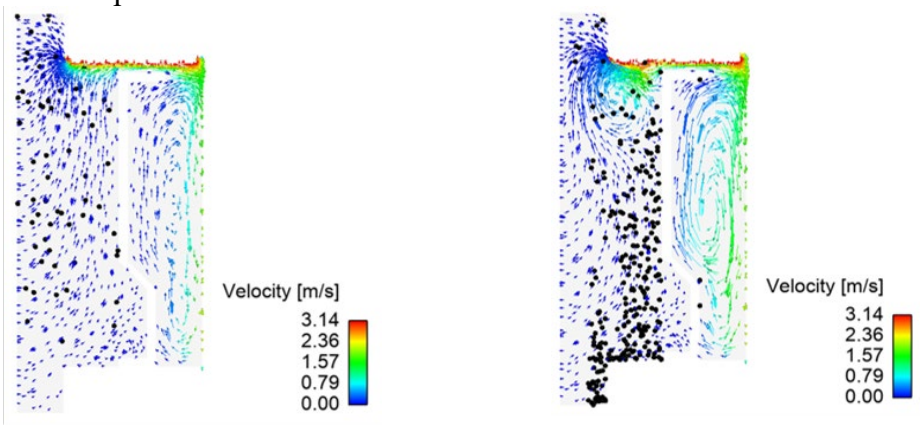

(a)t=0s (b)t=0.2s

Fig.4 Mechanism of gas-solid interaction

3 Numerical simulation of the fan-shaped bearing dust cover

3.1 Geometric model of the fan-shaped bearing dust cover

To enhance the dustproof performance of bearings and mitigate the negative influence of axial airflow velocity on dustproof performance, this study designed a fan-shaped bearing dust cover. The geometric model structure is shown in Fig.5(a). The entire fan-shaped bearing dust cover consists of four primary components: an outer cover plate, inner race, blades and filter mesh. The blade actively guides airflow patterns, while the filter mesh intercepts dust particles. Fig.5(b) shows the specific blade geometric structure.

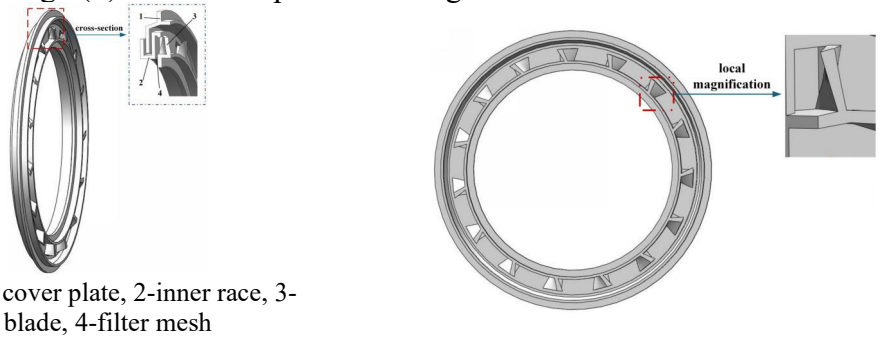

1-outer cover plate, 2-inner race, 3-blade, 4-filter mesh

(a) dust cover composition (b)blade

Fig.5 Geometric model of the fan-type bearing dust cover

3.2 Domain and mesh division of the fan-shaped bearing dust cover

The simulation process for the fan-shaped bearing dust cover involved domain and mesh division, consistent with the methodology applied to the standard bearing dust cover. As shown in Fig. 6(a), the fluid domain is divided into three main sections: a rotating domain, a stationary domain, and a porous media domain, with these domains connected via interfaces. Dust particles are generated in the bottom area outside the dust cover, while the filter mesh is modeled using the porous media model in Fluent software [17].

As shown in Fig. 8(b), tetrahedral meshing was implemented in Fluent Meshing with local refinement in the rotating domain to enhance mesh density, yielding a total of 1,029,329 elements that meet computational requirements.

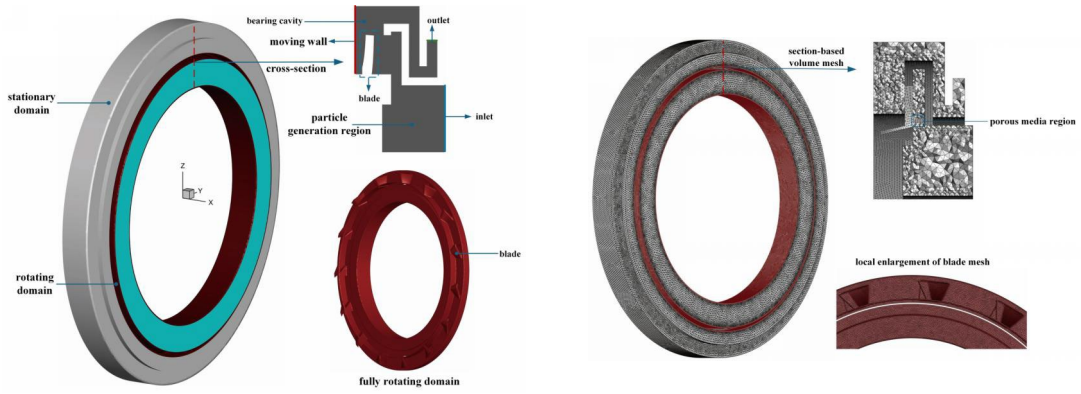

(a) Domain division (b) Mesh division

Fig.6 Domain and mesh division of the fan-shaped bearing dust cover

3.3 Solution settings of the fan-shaped bearing dust cover

Building on the previous simulation parameter selection, Fluent setup adopted a time step of 1×10^{-4} s with 2000 total iterations, data output interval of 20 steps with 0.2 s total simulation time. EDEM configured F240 white corundum dust particles with spherical morphology, using 21.25% of Rayleigh time. The time step for discrete element method was set to 1×10^{-6} s with data saved every 0.001 s. As shown in Table.5, key parameters remain consistent with conventional bearing dust cover simulations.

Table.5

Flow field and particle parameter settings of the fan-shaped bearing dust cover

Type	Item	Numerical value or Method
	Model	*RNG k-ε*
	Momentum	Second order upwind
	Wall	No slip

Flow field	Solver	Pressure-based
	Inlet	Velocity-inlet
	Outlet	Pressure-outlet
	Air inlet velocity (m/s)	0.01
	Rotational speed (rpm)	1000
Particle	Size (m)	4.5×10^{-5}
	Density (kg/m^3)	3900
	Shear modulus (MPa)	3.5×10^{4}
	Poisson's ratio	0.22
Wall	Density (kg/m^3)	7850
	Shear modulus (MPa)	8×10^{4}
	Poisson's ratio	0.31
Particle-particle	Coefficient of restitution	0.3
	Coefficient of static firction	0.5
	Coefficient of rolling firction	0.1
Particle-wall	Coefficient of restitution	0.5
	Coefficient of static firction	0.4
	Coefficient of rolling firction	0.05

3.4 Pressure distribution of the fan-shaped bearing dust cover

Fig. 7(a) shows the pressure distribution of the entire fluid domain induced by blade rotation in the bearing cavity. The rotating domain exhibits deep blue-colored negative pressure as blades continuously drive surrounding air inward, while the stationary domain above the blades displays red-colored high pressure due to external air influx compressing the domain. The substantial pressure differential with uniform distribution facilitates rapid airflow circulation, thereby enhancing dustproof performance. Fig. 7(b) shows a cross-sectional pressure contour, with the pressure distribution organized into two distinct areas: low-pressure areas 1, 2, 4 and high-pressure area 3. The low pressure in area 2 arises from blade rotation compressing air on the left side, resulting in reduced pressure on the blade's right flank. Continuous rotation of the bearing inner race drives the blades, forcing external airflow into the bearing cavity and causing progressive pressure buildup in area 3. The increasing pressure differential between areas 3 and 4 accelerates airflow from area 3 to 4. Simultaneously, as areas 1 and 4 communicate with ambient atmosphere, a recirculation loop forms from area 1 to 4.

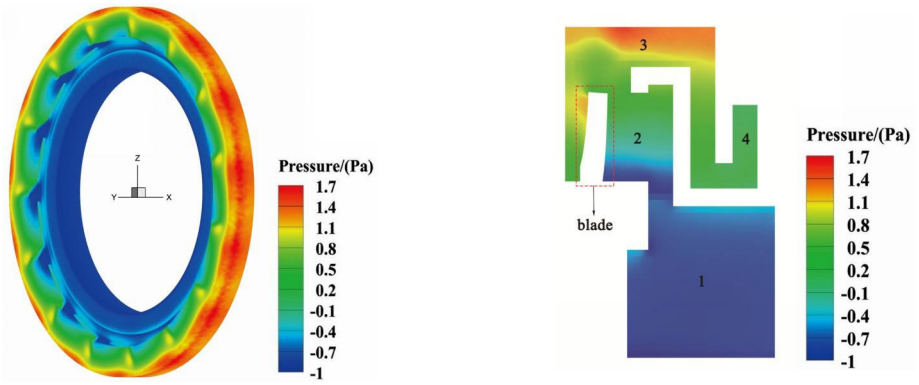

(a) Overall pressure contour (b) Cross-sectional pressure contour

Fig.7 Pressure distribution of the fan-type bearing dust cover

3.5 Velocity distribution of the fan-shaped bearing dust cover

Fig. 8(a) shows the cross-sectional velocity contour. In areas 2 and 3 ,the inner race drives the blade rotation, with area 2 exhibiting the highest velocity magnitude. Areas 1 and 4 are directly connected to the external environment, demonstrating significantly lower air velocities. In the filter mesh, the barrier effect of the filter mesh significantly impedes velocity propagation between both sides, resulting in a pronounced velocity gradient across the mesh. Fig. 8(b) shows the cross-sectional velocity vector plot. Arrow directions clearly indicate that airflow enters area 1 from the inlet, forms vortices driven by blade rotation, and air near the bearing inner race flows from area 1 to area 2 under negative pressure effects. The air in area 2 is split by the blades in area 3. A smaller portion flows downward along the left side, while the remainder escapes through the clearance of the dust cover to reach area 4, thereby forming a recirculation loop.

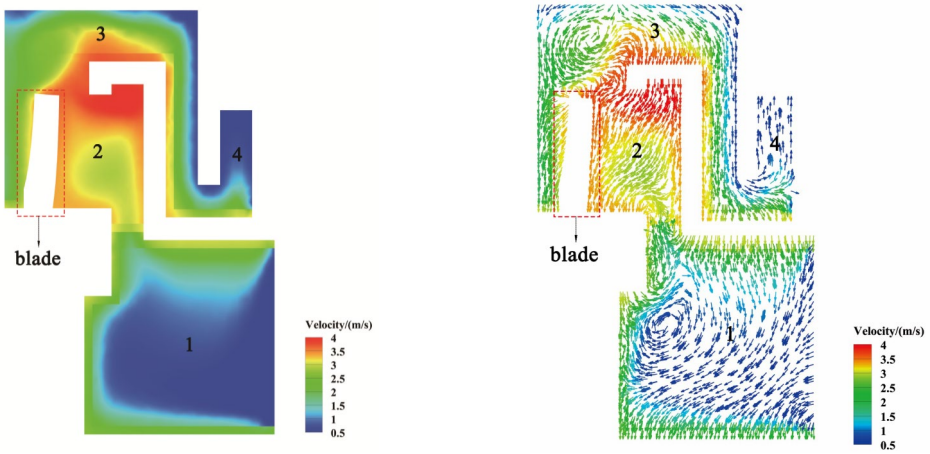

(a) Cross-sectional velocity Contour (b) Cross-sectional velocity vector plot

Fig. 8 Velocity distribution of the fan-shaped bearing dust cover

3.6 Particle trajectories

To clarify the dustproof principle of the fan-shaped bearing dust cover, motion analysis of particles was performed. Fig.9 shows dust particle trajectories under the cover's influence. At t=0.05 s, dust particles entering the dust cover exhibit low velocity dominated by gravitational settling, with a small fraction beginning to migrate toward the filter mesh. At t=0.1 s, dust particles become entrained by the rotating airflow of the inner race, exhibiting progressively increasing velocity. At t=0.15 s and t=0.2 s, particles increasingly concentrate in the filter mesh under combined vortical flow and centrifugal forces, with impeded horizontal motion inducing velocity decay at bearing cavity, culminating in gravitational settling to the simulated domain base.

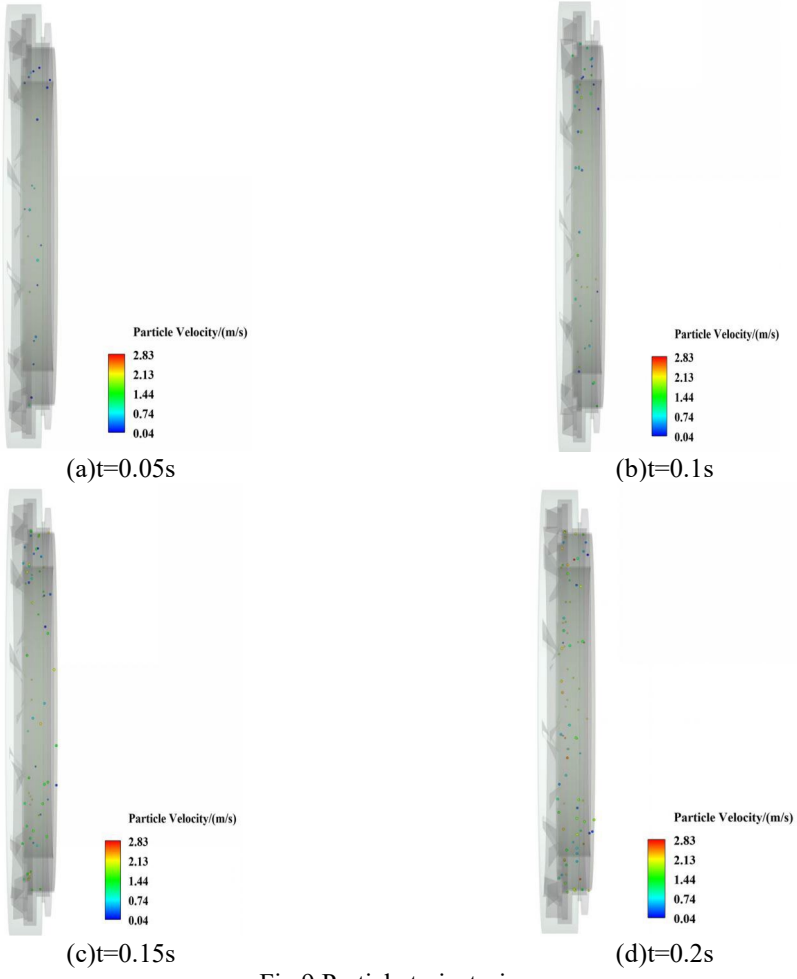

(a)t=0.05s (b)t=0.1s

(c)t=0.15s (d)t=0.2s

Fig.9 Particle trajectories

4 Material experiment

The fan-shaped bearing dust covers were manufactured via 3D printing using Model 9400 photosensitive resin, with dimensional tolerances maintained within ±0.1 mm. As shown in Fig.10, the physical model comprises blades and an outer cover plate, configured with dual geometric profiles to accommodate opposing bearing rotation directions. The blades are retrofitted with 10,000-mesh laboratory-grade nylon filters.

Fig.10 Physical model of the fan-shaped bearing dust cover

Dustproof experiment employed GB-standard 6210 single-row deep groove ball bearings with 50 mm nominal bore diameter. Fig. 11 demonstrates bearings equipped with different dust covers. Fig. 11(a) shows the 6210 bearing with a fan-shaped dust cover, while Fig. 11(b) shows the 6210-2Z bearing with a standard dust cover.

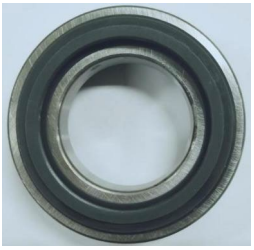

(a) 6210 bearing with a fan-type dust cover

(b) 6210-2Z bearing with a standard dust cover

Fig.11 Physical models of bearings with different dust covers

Dustproof experiment was conducted using the BGT-1A sealed bearing integrated experimenter evaluating dustproof performance, with overall dimensions of 670×480×1200mm. Experiment parameters consisted of a rotational speed of 1380 rpm, ambient temperature range of 10–30°C, and experimental period was set to 6 h. The dust material employed was white fused alumina powder F240, primarily composed of Al_2O_3 with particle size of 44.5 μm.

In dustproof performance experiment, bearing with the standard cover is designated as Bearing 1, and bearing with the fan-shaped dust cover is designated as Bearing 2. After the experiment, a preliminary analysis of the experiment samples was conducted. Fig.12 shows the appearance of the bearing grease after the experiment. Since the lubricating grease used in bearing 2 is blue, its internal

color is darker compared to bearing No. 1, which uses transparent lubricating grease.

(a) Bearing 1 Experiment Results

(b) Bearing 2 Experiment Results

Fig.12 Post-experiment appearance of two bearing types

To clearly compare dust ingress between the two bearings, Fig.13 shows post-experiment microscopic images of internal contamination. Bearing 1 exhibited extensive flaky dust particle accumulation, while bearing 2 equipped with a fan-shaped dust cover exhibited minimal dust particle intrusion into the cavity, showing sparse scattering. Under the same magnification, bearing 2 with a fan-shaped dust cover exhibits significantly superior dustproof performance compared to bearing 1.

Upon completion of the experiment, statistics of dust particles of both bear ing types were analyzed. The results showed that bearing 1 equipped with the stan dard dust cover exhibited a dust ingress concentration of 20,120 particles/cm³, whi le bearing 2 equipped with the cover fan-shaped dust cover demonstrated a signifi cantly lower particle concentration of 1,400 particles/cm³. The volumetric dust qu antity in the latter configuration measured merely 15% of that observed in bearing 1, indicating a remarkably effective dustproof performance. The implementation of fan-shaped bearing dust covers significantly mitigates dust accumulation within bearings, extending service life by 2-3 times and drastically reducing replacement frequency. Furthermore, it optimizes internal lubrication management, lowering l abor and consumable costs. Additionally, these designs enhance heat dissipation c apabilities to some extent, effectively reducing failure rates.

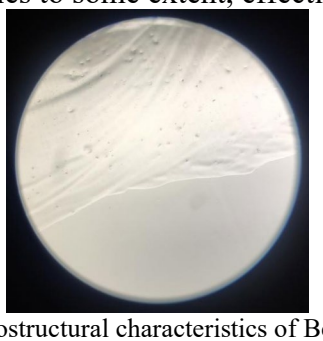

(a) Microstructural characteristics of Bearing 1

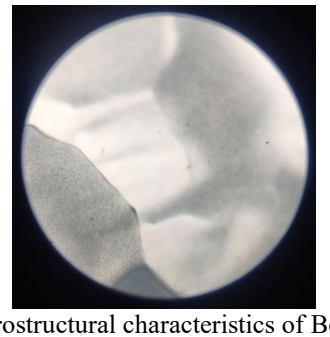

(b) Microstructural characteristics of Bearing 2

Fig.13 Microstructural characteristics of two bearing types

5 Conclusions

This study employed Fluent and EDEM software to establish a CFD-DEM coupling model integrating the internal flow field and particle field of bearing dust covers. The motion and distribution characteristics of dust particles under the blocking effect of the bearing dust cover were systematically simulated. Subsequently, the major factors influencing the dustproof performance during operational processes were analyzed. Addressing the identified key issues, a fan-shaped bearing dust cover was developed. Comprehensive numerical simulations and comparative material experiments yielded the following conclusions.

(1) An increase in air inlet velocity directly results in a significant rise in particle entering the bearing cavity. When the air inlet velocity reaches 0.01 m/s, the quantity of dust particles in the cavity becomes 16 times greater than that observed at the velocity of 0.001 m/s, substantially exceeding dust ingress under other conditions. Conversely, bearing rotational speed demonstrates a negative correlation with particle penetration. At a speed of 1000 rpm, the number of dust particles entering the cavity reaches 15 times that under higher rotational speeds.

(2) Dustproof failure mechanisms are primarily attributed to two aspects. Firstly, the complex force environment under combined gravitational and flow fields induces dispersed dust particles to accumulate near the clearance. Secondly, the axial velocity in the clearance drives these accumulated particles into bearing cavity, ultimately causing dustproof failures. Notably, the airflow axial velocity near the clearance was identified as the primary contributor to bearing dustproof failure.

(3) To address the adverse effects of axial airflow velocity on dustproof performance, a fan-shaped bearing dust cover was designed. Numerical simulations and material experiments demonstrate that the novel cover utilizes blades to guide disordered airflow of the bearing dust cover, creating an internal-external pressure differential and establishing an airflow recirculation loop. The filter mesh exhibits effective interception of dust particles, achieving significantly enhanced dustproof performance.

REFERENCES

[1] *Liu Jing, Dang Xiaoyong, Tang Changke, LI Xinbin, Pang Ruikun*. Failure mechanism analysis of aero-engine transmission bearings on multi-supporting platform[J]. Journal of Mechanical Engineering, Vol. **57**, Iss. 23, 2021,116-123.

[2] *Hao Y, Zhang C, Li X.* Research on defect detection method of bearing dust cover based on machine vision and multi-feature fusion algorithm[J]. Measurement Science and Technology, Vol. **34**, Iss. 10,2023, 105016.

[3] *Randall R B, Antoni J.* Rolling element bearing diagnostics-A tutorial[J]. Mechanical systems and signal processing, Vol. **25**, Iss. 2, 2011, 485-520.

[4] *Gegner J*. Tribological aspects of rolling bearing failures[J]. Tribology-lubricants and lubrication, 2011, 33-94.

[5] *Harris T A, Mindel M H.* Rolling element bearing dynamics[J]. Wear, Vol. **23**, Iss. 3,1973, 311-337.

[6] *Feng Ming, Hou Chong, Hu Minxue et al*. Analysis of motion and deposition of submicron particles in a gas dynamic bearing[J]. Chinese Journal of Inertial Technology, Vol. **27**, Iss. 2,2019, 227-234+240.

[7] *Wang Zhaoruijia, Zhang Xiaobin, LU Yongshuai et al.* Influence of ball rotation on the internal flow of lubrication under the ring of high-speed ball bearings[J]. Propulsion Technology, Vol. **43**, Iss. 9,2022, 319-327.

[8] *Chen Chao, Zhang Hong, Liu Qiuzhu*. Research on multiphase flowing water film carrying capacity of dynamic and static bearing based on CFD[J]. Lubrication and Sealing, Vol. **42**, Iss. 11,2017, 79-83.

[9] *Yu Y, Li X, Ren J, et al.* Influence of guide vane on dispersion of aggregates near the guide vane in a turbo air classifier[J]. Powder Technology, Vol. **434**, 2024, 119344.

[10] *El-Emam M A, Zhou L, Shi W, et al.* Theories and applications of CFD-DEM coupling approach for granular flow: A review[J]. Archives of Computational Methods in Engineering, 2021, 1-42e

[11] *Wang Xing, Zhang Ying, Ji Wenyi et al*. Operational dust characteristics of active anti-blocking no-till planter[J]. Journal of Agricultural Engineering, Vol. **39**, Iss. 2,2023, 14-23.

[12] *Zhang Hanzhong, Meng Wenjun, Wang Beibei*. Research on gas-solid two-phase flow field of grab discharge based on CFD-DEM coupled simulation[J]. Mining Research and Development, Vol. **42**, Iss. 4, 2022,166-172.

[13] *Feng D, Yangyang G, Liang W, et al*. EDEM-FLUENT coupled simulation of coal-gas outburst two-phase flow[J]. Energy Exploration Exploitation, Vol. **39**, Iss. 5,2021, 1786-1802.

[14] *Zhao Z, Zhou L, Bai L, et al.* Recent advances and perspectives of CFD-DEM simulation in fluidized bed[J]. Archives of Computational Methods in Engineering, Vol. **31**, Iss. 2, 2024,871-918.

[15] *Rejith R, Kesavan D, Chakravarthy P, et al*. Bearings for aerospace applications[J].Tribology International, Vol. **181**, 2023, 108312.

[16] *Dewen L I, Jinjun S U I, Guoqing L I U, et al.* Technical status and development direction of c oal mine dust hazard prevention and control technology in China[J]. Mining Safety & Enviro nmental Protection, Vol. **46**, Iss. 6, 2019,1-7, 13.

[17] *Seki A, Shirzadi M, Fukasawa T, et al.* Effect of filter microstructure on filtrationcharacteristic s in a nonwoven bag filter: A resolved CFD-DEM approach coordinated with X-ray computed tomography image[J]. Chemical Engineering Science, Vol. **299**, 2024, 120533.